



HAL
open science

Crystallization of polymers under strain : from molecular properties to macroscopic models

Arnaud Poitou, Amine Ammar, Yann Marco, L. Chevalier, Mohend Chaouche

► **To cite this version:**

Arnaud Poitou, Amine Ammar, Yann Marco, L. Chevalier, Mohend Chaouche. Crystallization of polymers under strain : from molecular properties to macroscopic models. *Computer Methods in Applied Mechanics and Engineering*, 2003, 192 (28 30), pp.3245-3265. 10.1016/S0045-7825(03)00349-9. hal-01006710

HAL Id: hal-01006710

<https://hal.science/hal-01006710>

Submitted on 6 Feb 2017

HAL is a multi-disciplinary open access archive for the deposit and dissemination of scientific research documents, whether they are published or not. The documents may come from teaching and research institutions in France or abroad, or from public or private research centers.

L'archive ouverte pluridisciplinaire **HAL**, est destinée au dépôt et à la diffusion de documents scientifiques de niveau recherche, publiés ou non, émanant des établissements d'enseignement et de recherche français ou étrangers, des laboratoires publics ou privés.



Distributed under a Creative Commons Attribution 4.0 International License

Crystallization of polymers under strain: from molecular properties to macroscopic models

A. Poitou ^a, A. Ammar ^b, Y. Marco ^c, L. Chevalier ^c, M. Chaouche ^c

^a *Ecole Centrale de Nantes, BP 92101 F-44321, Nantes Cedex 3, France*

^b *Laboratoire de Rhéologie, 1301 rue de la piscine, BP 53 Domaine universitaire, 38041 Grenoble Cedex 9, France*

^c *LMT, ENS de Cachan, 61 Avenue du Président Wilson, 94235 Cachan, France*

The crystallization of thermo-plastic polymers under strain is considered both theoretically and experimentally. The thermo-mechanical model presented here is performed in the framework of the so-called generalized standard materials. In our model we couple in a very natural way the kinetics of crystallization with the mechanical history experienced by the polymer. The viscoelastic properties of the polymer are described using molecular theories. Therefore, in this model of strain-induced crystallization, the kinetics of crystallization is explicitly linked to the polymer chain conformation. Our model is intended to be valid for both for shearing and elongation, or any other complex strain field. Two different viscoelastic molecular models are considered here, corresponding to Maxwell and Pom–Pom constitutive equations. The model is implemented in a dedicated finite element code and the case of injection molding is considered.

To validate our strain-induced crystallization model, which explicitly takes into account the molecular conformation, experiments investigating the material behavior at the molecular scale are required. Several measurement techniques can be used to achieve this task, including infrared spectroscopy, optical polarimetry, X-ray scattering or diffraction, etc. In this paper, the wide angle X-ray diffraction (WAXD) is used to investigate the crystalline texture of the polymer. We consider here the case of poly(ethylene terephthalate) (PET) subjected to a biaxial elongation above its T_g . The strain field is determined using a home-developed image correlation technique that allows us to infer all the strain components at each point of the specimen, even in the case of a non-homogeneous strain field. To minimize the effect of quiescent crystallization, specimens are quickly heated with infrared and the temperature was regulated during the test. At the end of the deformation process, the specimens were quenched to room temperature. Their microstructure was later investigated using the WAXD technique. In order to undertake local and accurate WAXD measurements Synchrotron radiation facilities are used.

Keywords: Crystallization; Thermo-mechanical; Molecular model; X-ray diffraction

Notations

M	tensorial notation (M_{ij})
$\underline{\underline{M}} : \underline{\underline{N}}$	trace of the matricial product ($\text{Tr}(\underline{\underline{M}} \cdot \underline{\underline{N}})$ or $M_{ij}N_{ij}$)
t	intrinsic time
d/dt	time material derivative
$\partial/\partial t$	time partial derivative
$\delta/\delta t$	time upper convective derivative
$\tilde{D}/\tilde{D}t$	general notation for a convective derivative
X	thermodynamic internal variable
Y	thermodynamic dual variable
ϕ	intrinsic dissipation
ψ	free energy (indices “c” and “a” are relative to crystalline and amorphous phase)
φ^*	dissipation pseudopotential (index “N” refers to quiescent (natural) crystallization and index “M” stands for mechanical dissipation)
ρ_0	density
$\underline{\underline{\tau}}$	extra stress tensor
$\underline{\underline{D}}$	strain rate tensor ($D_{ij} = (v_{i,j} + v_{j,i})/2$)
n, χ	kinetic parameters
T	temperature
L	latent heat
x	degree of crystallinity
x_∞	ultimate degree of crystallinity
α	relative crystallinity
f	intrinsic crystallinity
β	dual variable of relative crystallinity
Λ	dual variable of intrinsic crystallinity
$\underline{\underline{c}}$	conformation tensor
$\underline{\underline{z}}$	dual variable of conformation tensor
G	elastic shear modulus
$\underline{\underline{\varepsilon}}$	elastic strain tensor for infinite strains
$\underline{\underline{Y}}$	dual variable of elastic strain tensor
m, K	power-law behaviour materials constants
η	viscosity
θ	relaxation time
νK	number of chains per unit volume multiplied by dumbbell stiffness
$\underline{\underline{v}}$	velocity field
G_0, ϕ_b	material parameter of the Pom–Pom model
λ	chain stretch
$\underline{\underline{S}}$	chain orientation tensor
μ	dual variable of chain stretch
$\underline{\underline{y}}$	dual variable of chain orientation tensor
θ_s	stretch relaxation time
θ_b	backbone relaxation time

1. Introduction

A number of thermo-plastic polymers, in particular those presenting stereoregularity, can partially crystallize between their glass transition temperature (T_g) and their melting temperature. Under quiescent state conditions, the crystallization kinetics is well described by Avrami-type models, and a number of related studies have been reported in the literature. However, in most of practical situations, during processing for instance, the polymer experiences both mechanical and thermal solicitations. In this case, polymer crystallization leads to spontaneous formation of a nanocomposite structure in which plate-like crystals that give strength are separated by non-crystalline material that confers toughness. This is taken as an advantage to make easier some polymer processing operations such as spinning, and to avoid some mechanical instabilities (necking for instance).

In spite of its industrial relevance, the problem of polymer crystallization under flow conditions is far to be understood, and nowadays the problem of modelling this process, taking into account experimental observations at molecular level, remains open. The purpose of the study reported here is two-fold. First, a tentative modelling of thermo-mechanical behaviour of polymers taking into account crystallization is presented. This model is developed in the thermodynamic framework of so-called "standard materials", in which we explicitly take into account results of molecular theories [1]. Secondly, some experimental results based on the X-ray diffraction technique are presented, in which data at molecular level can be inferred [2]. The comparison between experimental results and numerical simulations based on the model developed here is still under investigation and will be reported elsewhere.

In most existing theories (see [3–5] for example), flow-induced crystallization is modelled with two independent steps. In a first one, kinetics laws are parameterised by flow conditions (shear or elongation) and independently, or in a second step, the mechanical materials properties (viscosity, relaxation time...) are parameterised by the degree of crystallinity. Our point of view is similar to the one developed by Doufas et al. [6]. We believe that it is possible to model flow-induced crystallization in the framework of irreversible thermodynamics. This means in particular that the two above-mentioned steps are in fact not independent (in analogy with Onsager's reciprocal relations). The advantage of this type of modelling is that thermodynamics equations are relatively easy to implement in finite element packages and then deal with practical situations (complex geometries).

In the second part of this paper some experimental results are presented, in which the microstructure of the polymer previously subjected to thermo-mechanical solicitations is analyzed. We consider here the case of poly(ethylene terephthalate) (PET), which is often used to manufacture carbonated beverage bottles and some household cleanser containers. X-ray diffraction provides one of the most powerful techniques for characterizing a crystalline texture, and this is the technique used here. Considerable work has been undertaken to investigate the effects of strain on the crystallization of PET above and close to its T_g using X-ray scattering. Ex situ [7,8] as well as in situ synchrotron experiments [9,10] have been reported. In these studies, the influence of several parameters has been considered, including the draw rate, the draw ratio and the temperature. In the study presented here, the microstructure was analysed ex situ, i.e. after both stretching and relaxation. In most of the experiments reported in the literature on strain-induced crystallization, the stretching tests are uniaxial. However, in a real industrial process, such as blow moulding, the polymer is often subjected to a much more complex strain field than in simple uniaxial drawing. Due to the high anisotropy of polymer chains, the type of deformation would affect the microstructure crucially. Multi-axial deformations are actually very difficult to perform tidily and are quite rare. Here, 'real' biaxial tests are carried out using a tri-axial test machine. In order to ensure a rapid and uniform heating of the specimens above the polymer's T_g , we used an infra-red heating apparatus. The local stress is not measured here, but the strain field is determined using an image correlation technique.

2. Theoretical section

2.1. Generalized standard materials

The standard material formalism has been extensively used in solid mechanics to describe elasticity, plasticity, damage as well as many different coupled phenomena. We give here a new extension of this formalism, which enables us to account for molecular parameters (conformation tensor, tube orientation or extension . . .) in finite strains.

The main idea of this formalism is that two potentials are required to describe the behaviour of a material. The first one is a thermodynamic potential (specific Gibbs free energy ψ for example), which allows us to quantify the ability of the material to store energy. The second one is called a pseudopotential, which allows us to quantify the ability of the material to dissipate energy. The general procedure is the following:

Step 1: Identify which material parameters \underline{X} ¹ to use to describe the storage of energy. Then quantify this energy, (i.e. give a mathematical expression for $\psi(\underline{X})$) and calculate the dual variable $\underline{Y} = \rho_0 \partial\psi / \partial\underline{X}$.

Step 2: Identify a material derivative $\tilde{D}/\tilde{D}t$. This derivative is chosen so that for reversible processes (i.e. for short experimental time scales compared to materials relaxation times), $\tilde{D}\underline{X}/\tilde{D}t = \underline{0}$. Then, if we write the specific dissipation $\phi = \underline{\tau} : \underline{D} - \underline{Y} \cdot d\underline{X}/dt$ and we note that this dissipation must be zero as soon as the process is reversible (i.e. as soon as $\tilde{D}\underline{X}/\tilde{D}t = \underline{0}$), we obtain an expression for the extra stress tensor $\underline{\tau}$.

Step 3: Identify a dissipation pseudopotential $\varphi^* = \varphi^*(\underline{Y})$ such that the evolution equations write $\tilde{D}\underline{X}/\tilde{D}t = -\partial\varphi^*/\partial\underline{Y}$.² In order to satisfy the second law of thermodynamics (Clausius Duhem inequality), this potential is assumed to be convex such that $\varphi^*(\underline{Y} = \underline{0}) = 0$. The derivation of this pseudopotential is not always obvious, but from known constitutive relations it is usually possible to find it out.

This formalism allows us to extend the mechanical constitutive relation and to account for different coupling phenomena like induced crystallization.

2.2. Induced crystallization—general framework

2.2.1. Quiescent crystallization

Noting x and x_∞ the actual and ultimate degree of crystallinity, $\psi_c(T)$ (resp. $\psi_a(T)$) the free energy for a purely crystalline (resp. purely amorphous) phase, L the latent heat of crystallization, noting n (resp. $\chi(T)$) an adjustable scalar (resp. function of temperature), it can be shown [10] that Nakamura quiescent crystallization kinetics (1) and (2) can be put into the standard form (3) and (4).

$$\alpha = \frac{x}{x_\infty} = 1 - \exp(-f), \quad (1)$$

$$\frac{df}{dt} = \frac{nf^{n-1}}{\chi(T)}, \quad (2)$$

$$\psi_N(T, f) = (1 - \exp(-f))x_\infty\psi_c(T) + (1 - (1 - \exp(-f))x_\infty)\psi_a(T), \quad (3)$$

$$A = \rho_0 \frac{\partial\psi_N}{\partial f} = \exp(-f)x_\infty(\psi_a(T) - \psi_c(T)) = \beta(T) \exp(-f) \approx Lx_\infty \left(1 - \frac{T}{T_m}\right) \exp(-f) \quad (4)$$

¹ \underline{X} can be either a set of scalar, vector or tensor variables.

² $\partial\varphi^*/\partial\underline{Y}$ is a kind of generalization of the M matrix of the GENERIC formalism.

and thus

$$-\frac{\partial \varphi_N^*(A)}{\partial A} = \frac{n}{\chi(T)} \left[\ln \left(\frac{\beta(T)}{A} \right) \right]^{1-\frac{1}{n}}. \quad (5)$$

2.2.2. Flow-induced crystallization

A ‘‘natural’’ model for induced crystallization consists in simply adding the different potentials (index M referring to mechanical constitutive behaviour and index N to Nakamura’s kinetics). The coupling is achieved essentially by the fact that the mechanical parameters depend on the degree of crystallinity.

$$\psi = \psi(T, f, \underline{\underline{\varepsilon}}) = \psi_N(T, f) + \psi_M^{(f)}(\underline{\underline{\varepsilon}}), \quad (6)$$

$$\varphi^* = \varphi_N^*(T, A) + \varphi_M^{*(A)}(\underline{\underline{\varepsilon}}). \quad (7)$$

Superscripts (f) and (A) mean that the rheological parameters (Maxwell relaxation time and viscosity for example) are parameterised by the degree of crystallinity. Governing equations are deduced from (6) and (7) by following the three above-mentioned steps. In particular, kinetics of crystallization writes:

$$\dot{f} = -\frac{\dot{A}}{A} = -\frac{\partial}{\partial A} \left(\varphi_N^*(T, A) + \varphi_M^{*(A)}(\underline{\underline{\varepsilon}}) \right). \quad (8)$$

2.3. Flow-induced crystallization for a power-law viscous fluid

A power-law viscous fluid is modelled here as a viscoelastic fluid undergoing very small elastic strains $\underline{\underline{\varepsilon}}$.
Step 1:

$$\psi_M = \psi_M(T, \underline{\underline{\varepsilon}}) = \frac{G}{2} \left(\underline{\underline{\varepsilon}} : \underline{\underline{\varepsilon}} \right), \quad (9)$$

$$\underline{\underline{Y}} = \frac{\partial \psi_M}{\partial \underline{\underline{\varepsilon}}} = G \underline{\underline{\varepsilon}}. \quad (10)$$

Step 2: If $\underline{\underline{D}}$ denotes the strain rate tensor

$$\frac{\tilde{D} \underline{\underline{\varepsilon}}}{\tilde{D} t} = \frac{d \underline{\underline{\varepsilon}}}{dt} - \underline{\underline{D}} \approx -\underline{\underline{D}}. \quad (11)$$

The dissipation writes then

$$\phi = \underline{\underline{\tau}} : \underline{\underline{D}} - \underline{\underline{Y}} : \frac{d \underline{\underline{\varepsilon}}}{dt} = (\underline{\underline{\tau}} - \underline{\underline{Y}}) : \underline{\underline{D}} - \underline{\underline{Y}} : \frac{\tilde{D} \underline{\underline{\varepsilon}}}{\tilde{D} t}. \quad (12)$$

Leading to

$$\underline{\underline{\tau}} = \underline{\underline{Y}} = G \cdot \underline{\underline{\varepsilon}}.$$

Step 3:

$$\varphi_M^*(\underline{\underline{\tau}}) = \frac{m}{2^{m+1/2m} (m+1) K^{1/m}} (\underline{\underline{\tau}}^d : \underline{\underline{\tau}}^d)^{m+1/2m}, \quad (13)$$

where $\underline{\underline{\tau}}^d$ denotes the deviator of $\underline{\underline{\tau}}$ ($\tau_{ij}^d = -\tau_{kk} \delta_{ij} + \tau_{ij}$).

So that the constitutive law is classically written, in neglecting the elastic strains

$$\frac{\tilde{D}\underline{\underline{\epsilon}}}{D\underline{\underline{t}}} = \frac{d\underline{\underline{\epsilon}}}{dt} - \underline{\underline{D}} = -\frac{\partial\varphi_M^*}{\partial\underline{\underline{\tau}}} \Rightarrow \underline{\underline{\tau}}^d \approx 2K(2\underline{\underline{D}} : \underline{\underline{D}})^{m-1/2}\underline{\underline{D}}. \quad (14)$$

Step 4: Assuming that m is not affected by crystallization, Eq. (8) then writes:

$$\frac{df}{dt} = \frac{n}{\lambda(T)} \left[\ln \left(\frac{\beta(T)}{A} \right) \right]^{1-\frac{1}{n}} - \frac{m}{2^{m+1/2m}(m+1)} (\underline{\underline{\tau}}^d : \underline{\underline{\tau}}^d)^{m+1/2m} \frac{d}{dA} \left(\frac{1}{K(A)^{1/m}} \right). \quad (15)$$

2.3.1. Discussion

As a consequence of a kind of Onsager principle, the influence of flow on crystallization is completely determined by the influence of crystallization on the flow (i.e. by the way the rheological parameters depend on crystallinity through A).

- In the Newtonian case ($m = 1$, $K = \eta$), the equations are explicit. As A is an increasing function of the crystallinity α , it can be seen that there is two mechanisms for crystallization. The first one has a thermal origin and is correctly described by the Nakamura law. The second one has a mechanical origin: as soon as the viscosity depends on A and as the thermal crystallization is not instantaneous, there is a crystallization induced by the flow. This dependence is equivalent to a dependence of the viscosity on α . An illustration of this point is found on two different rheological tests assumed to be carried out with polymers of different molecular length. In the first test we consider a shearing experiment carried out at a constant shear rate. The viscosity is proportional to the molecular length to a power of 3.4, thus one can deduce from (15), that the longer the molecule is, the more effective is the flow-induced crystallization. In a second test, we consider a shear experiment, which is carried out at a constant shear stress. The viscosity is then put at the denominator, which induces an opposite influence: the longer the molecule is, the less important is the induced crystallization.
- Fig. 1 depicts the evolution of the shear viscosity with respect to time in a test carried out at a constant temperature and shear rate. The function $K(A)$ is adjusted to fit at best the experiments of Titomanlio and Speranza [4] (Fig. 2). The qualitative evolution of viscosity with time is correctly predicted. It can also be noted from Fig. 3 that, even though no induction time has been artificially introduced into the model, an apparent induction time is correctly predicted: the crystallization seems to take place after a certain time only, and this induction time appears to be a decreasing function of strain rate.

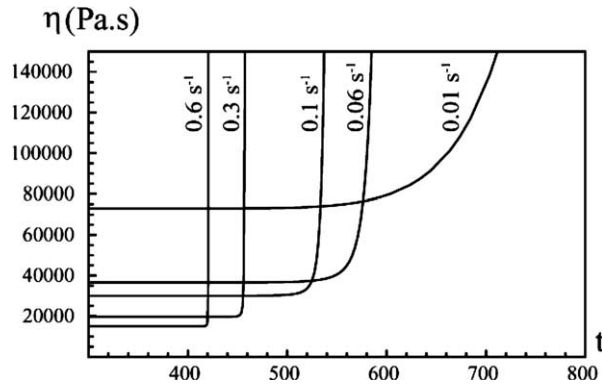


Fig. 1. Numerical predictions for increase of shear viscosity due to crystallization.

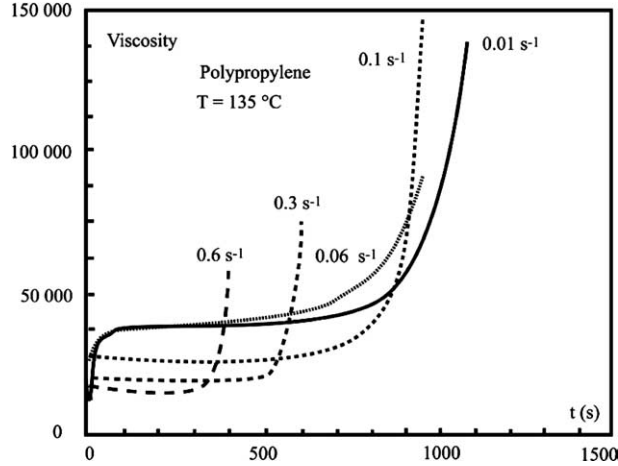


Fig. 2. Experimental increase of shear viscosity due to crystallization.³

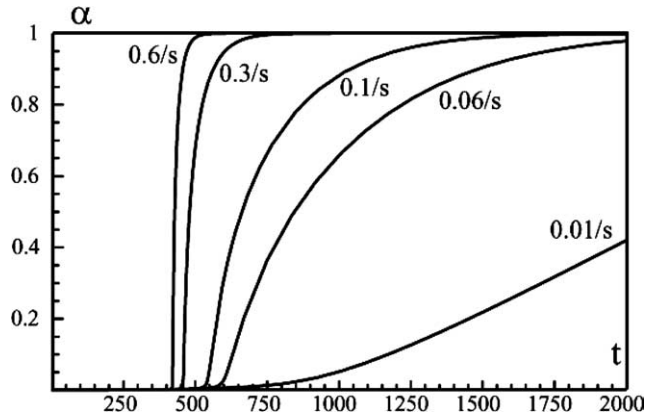


Fig. 3. Crystallinity induced by flow at different shear rates.

2.4. Flow-induced crystallization for a viscoelastic fluid

2.4.1. Upper convected Maxwell fluid

If K denotes the elastic stiffness of the dumbbell, v the number of chains per unit volume, G the elastic modulus of the Maxwell fluid and $\delta/\delta t$ the upper convected derivative, then the evolution of the conformation tensor ($\underline{c} = \langle \underline{R} \cdot \underline{R} \rangle$ where \underline{R} denotes the end-to-end vector of the polymeric chain) is given by

$$\frac{\delta \underline{c}}{\delta t} = -\frac{1}{\theta} \underline{c} + \frac{G}{\theta v K} \underline{1}, \quad (16)$$

where $\delta/\delta t$ denotes the upper convected derivative

$$\frac{\delta \underline{c}}{\delta t} = \frac{d \underline{c}}{d t} - \underline{\text{grad}} \underline{v} \cdot \underline{c} - \underline{c} \cdot \underline{\text{grad}} \underline{v}^T. \quad (17)$$

³ Experimental results from Titomenlio and Speranza [4].

So that, if $\underline{\underline{D}}$ denotes the strain rate tensor, the extra stress tensor writes

$$\underline{\underline{\tau}} = vK\underline{\underline{c}} - G\underline{\underline{1}} \quad (18)$$

with

$$\frac{\delta \underline{\underline{\tau}}}{\delta t} + \underline{\underline{\tau}} = 2\eta \underline{\underline{D}} \quad \text{and} \quad 2\eta = G\theta. \quad (19)$$

Step 1: The free energy depends on temperature T and conformation tensor $\underline{\underline{c}}$. So that, in neglecting thermo-elasticity:

$$\rho_0 \psi_M(\underline{\underline{c}}) = \frac{1}{2} \left[vK \text{Tr}(\underline{\underline{c}}) - G \ln(\det(\underline{\underline{c}})) \right], \quad (20)$$

$$\underline{\underline{z}} = \rho_0 \frac{\partial \psi_M}{\partial \underline{\underline{c}}} = \frac{1}{2} \left[vK\underline{\underline{1}} - G\underline{\underline{c}}^{-1} \right].$$

Step 2: For the upper convected Maxwell model, the derivative $\tilde{D}/\tilde{D}t$ is the upper convected one, so that a deformation is elastic if and only if $\delta \underline{\underline{c}}/\delta t = 0$. The dissipation writes then

$$\phi = (\underline{\underline{\tau}} - 2\underline{\underline{z}} \cdot \underline{\underline{c}}) \underline{\underline{D}} - \underline{\underline{z}} : \delta \underline{\underline{c}}/\delta t. \quad (21)$$

So that the expression for the extra stress tensor is deduced as:

$$\underline{\underline{\tau}} = 2\underline{\underline{z}} \cdot \underline{\underline{c}}. \quad (22)$$

Step 3: The pseudopotential is given by:

$$\varphi_M^*(\underline{\underline{z}}) = -\frac{G}{2\theta} \ln \det \left(1 - \frac{2}{vK} \underline{\underline{z}} \right) - \frac{G}{vK\theta} \text{Tr}(\underline{\underline{z}}). \quad (23)$$

So that

$$\frac{\tilde{D}\underline{\underline{c}}}{\tilde{D}t} = \frac{\delta \underline{\underline{c}}}{\delta t} = -\frac{\partial \varphi^*}{\partial \underline{\underline{z}}} = -\frac{1}{\theta} \underline{\underline{c}} + \frac{G}{\theta vK} \underline{\underline{1}}. \quad (24)$$

It is then straightforward to verify that Eqs. (20), (22) and (23) yield to the classical expression (19) for the upper convected Maxwell model.

Step 4: In assuming that the relaxation time depends predominantly on crystallinity, Eq. (12) then writes:

$$\frac{df}{dt} = \frac{n}{\lambda(T)} \left(\ln \left(\frac{\beta}{A} \right) \right)^{1-\frac{1}{n}} + \frac{\partial}{\partial A} \left(\frac{1}{\theta(A)} \right) \left(\frac{G}{2} \ln \det \left(1 - \frac{2}{vK} \underline{\underline{z}} \right) + \frac{G}{vK} \text{Tr}(\underline{\underline{z}}) \right). \quad (25)$$

But

$$\underline{\underline{z}} = \frac{1}{2} vK \underline{\underline{1}} - \frac{1}{2} vK \left(\frac{\underline{\underline{\tau}}}{G} + \underline{\underline{1}} \right)^{-1}. \quad (26)$$

So that

$$\frac{df}{dt} = \frac{n}{\lambda(T)} \left(\ln \left(\frac{\beta}{A} \right) \right)^{1-\frac{1}{n}} - \frac{\partial}{\partial A} \left(\frac{1}{\theta(A)} \right) \left(\frac{G}{2} \ln \det \left(\frac{\underline{\underline{\tau}}}{G} + \underline{\underline{1}} \right) + \frac{G}{2} \text{Tr} \left(\left(\frac{\underline{\underline{\tau}}}{G} + \underline{\underline{1}} \right)^{-1} - 3 \right) \right). \quad (27)$$

2.4.2. Pom–Pom model [11]

The Pom–Pom model exhibits two relaxation mechanisms: tube orientation $\underline{\underline{S}}$ and backbone stretch λ . In its differential form, it can be written

$$\underline{\underline{\tau}} = \frac{15}{4} G_0 \phi_b^2 \lambda^2 \underline{\underline{S}}, \quad (28)$$

$$\frac{d\underline{\underline{S}}}{dt} = \underline{\underline{\text{grad}}} v \cdot \underline{\underline{S}} + \underline{\underline{S}} \cdot \underline{\underline{\text{grad}}} v^T - 2(\underline{\underline{S}} : \underline{\underline{D}})\underline{\underline{S}} - \frac{1}{\theta_b} \left(\underline{\underline{S}} - \frac{1}{3} \underline{\underline{1}} \right), \quad (29)$$

$$\frac{d\lambda}{dt} = \lambda(\underline{\underline{S}} : \underline{\underline{D}}) - \frac{1}{\theta_s} (\lambda - 1). \quad (30)$$

Step 1: The free energy depends on $\underline{\underline{S}}$ and λ and can be written, following Öttinger expression for the entropy [13]:

$$\rho \psi_M(T, \lambda, \underline{\underline{S}}) = -\frac{1}{6} H \ln \det \underline{\underline{S}} + \frac{1}{2} H (\lambda^2 - 2 \ln(\lambda)), \quad (31)$$

$$\text{with } H = \frac{15}{4} G_0 \phi_b^2, \quad (32)$$

$$\text{associated dual variables are } \underline{\underline{y}} = \rho_0 \frac{\partial \Psi}{\partial \underline{\underline{S}}} = -\frac{1}{6} H \underline{\underline{S}}^{-1}, \quad (33)$$

$$\mu = \rho_0 \frac{\partial \psi}{\partial \lambda} = H \left(\lambda - \frac{1}{\lambda} \right). \quad (34)$$

Step 2: The derivative $\tilde{D}/\tilde{D}t$ is defined by

$$\frac{\tilde{D}}{\tilde{D}t} \left(\frac{\underline{\underline{S}}}{\lambda} \right) = \left(\frac{\frac{\Delta \underline{\underline{S}}}{\Delta t}}{\frac{\tilde{\delta} \lambda}{\tilde{\delta} t}} \right) = \left(\frac{\frac{d\underline{\underline{S}}}{dt} - \underline{\underline{\text{grad}}} v \cdot \underline{\underline{S}} - \underline{\underline{S}} \cdot \underline{\underline{\text{grad}}} v^T + 2(\underline{\underline{S}} : \underline{\underline{D}})\underline{\underline{S}}}{\frac{d\lambda}{dt} - \lambda(\underline{\underline{S}} : \underline{\underline{D}})} \right), \quad (35)$$

$\Delta/\Delta t$ is a convective derivative preserving the trace, which is “naturally” associated to the upper convected derivative $\delta/\delta t$ for a tensor of trace unity ($\text{Tr}(\underline{\underline{S}}) = S_{kk} = 1$). More precisely

$$\frac{\Delta \underline{\underline{S}}}{\Delta t} = \frac{\delta \underline{\underline{S}}}{\delta t} - \text{Tr} \left(\frac{\delta \underline{\underline{S}}}{\delta t} \right) \frac{\underline{\underline{S}}}{\text{Tr}(\underline{\underline{S}})} \quad \text{so that} \quad \text{Tr} \left(\frac{\Delta \underline{\underline{S}}}{\Delta t} \right) = 0. \quad (36)$$

The dissipation writes then

$$\phi = \underline{\underline{\tau}} : \underline{\underline{D}} - \underline{\underline{y}} : \frac{d\underline{\underline{S}}}{dt} - \mu \frac{d\lambda}{dt}. \quad (37)$$

Or, with Eqs. (33)–(35)

$$\phi = \left[\left(\underline{\underline{\tau}} - H \lambda^2 \underline{\underline{S}} + \frac{H}{3} \underline{\underline{1}} \right) : \underline{\underline{D}} \right] - \underline{\underline{y}} : \frac{\Delta \underline{\underline{S}}}{\Delta t} - \mu \frac{\tilde{\delta} \lambda}{\tilde{\delta} t}. \quad (38)$$

$$\text{But } \frac{\Delta \underline{\underline{S}}}{\Delta t} = 0 \quad \text{and} \quad \frac{\tilde{\delta} \lambda}{\tilde{\delta} t} = 0 \Rightarrow \phi = 0, \quad (39)$$

$$\text{Thus } \underline{\underline{\tau}} = H \lambda^2 \underline{\underline{S}} - \frac{H}{3} \underline{\underline{1}}. \quad (40)$$

Step 3:

$$\varphi_M^*(\underline{y}, \mu) = \frac{1}{\theta_b} \left[-\frac{H}{6} \ln \left(\det \left(\frac{-2\underline{y}}{H} \right) \right) - \frac{1}{3} \text{Tr}(\underline{y}) - \frac{H}{2} \right] + \frac{1}{\theta_s} \left[\int_0^\mu \frac{m}{H} - 1 + \sqrt{1 + \left(\frac{m}{H} \right)^2} dm \right]. \quad (41)$$

It is then straightforward to verify that Eqs. (33)–(35) and (41) yield the classical expression (28)–(30) for the Pom–Pom model.

Step 4: In assuming that the relaxation time depends predominantly on crystallinity, Eq. (12) then writes:

$$\begin{aligned} \dot{f} = & -\frac{\partial}{\partial \lambda} \left(\frac{1}{\theta_b(\lambda)} \right) \left(-\frac{H}{6} \ln \det \frac{-2\underline{y}}{H} - \frac{1}{3} \text{Tr}(\underline{y}) - \frac{H}{2} \right) \\ & - \frac{\partial}{\partial \lambda} \left(\frac{1}{\theta_s(\lambda)} \right) \int_0^\mu \frac{m}{H} - 1 + \sqrt{1 + \left(\frac{m}{H} \right)^2} dm + \frac{n}{\chi(T)} \left(\ln \left(\frac{\beta}{\lambda} \right) \right)^{1-\frac{1}{n}}. \end{aligned} \quad (42)$$

2.5. Numerical simulation

2.5.1. Algorithm

For sake of simplicity, we describe here the algorithm for an isothermal flow. We look for a numerical solution of a problem on a domain Ω (whose boundary is denoted by Γ) with the traction null on the flow front Γ_1 and with the velocity $\underline{v} = \underline{v}_g$ on the inlet Γ_2 . Through Γ_2 the polymer is introduced into the domain and we impose an orientation tensor $\underline{\underline{S}}$, a stretch λ , a degree of crystallinity α (or equivalently f) and a velocity vector \underline{v}_g . On the boundary $\Gamma_0 = \Gamma - \Gamma_1 \cup \Gamma_2$ we assume that $\underline{v}_g = \underline{0}$ (no slip condition).

The problem is defined as:

Find $(\underline{v}, \underline{\underline{t}}, \underline{\underline{S}}, \lambda, f)$ satisfying simultaneously the constitutive relations (28)–(30), (32)–(34) and (42) as well as kinematics and static admissibility.

- *Kinematics admissibility*

$$\underline{v} = \underline{v}_g \quad \text{on } \Gamma_2, \quad (43)$$

$$\text{Div } \underline{v} = \underline{0} \quad \text{in } \Omega. \quad (44)$$

- *Static admissibility*

$$\underline{\underline{\sigma}} \underline{n} = \underline{0} \quad \text{on } \Gamma_1, \quad (45)$$

$$\text{Div } \underline{\underline{\sigma}} = \underline{0} \quad \text{in } \Omega. \quad (46)$$

- *Inflow boundary condition*

$$\underline{\underline{S}} = \underline{\underline{S}}^0, \quad \lambda = \lambda_0, \quad \text{and} \quad f = f_0 \quad \text{on } \Gamma_2. \quad (47)$$

We solve these equations with a decoupled algorithm. In a first step, we assume that the internal variables f , $\underline{\underline{S}}$, λ as well as the geometrical domain occupied by the polymer are known. We solve then the resulting equations with a DEVSS algorithm which lead to the velocity field at each point of the domain. We then actualize f , $\underline{\underline{S}}$, λ with a discontinuous Taylor Galerkin method and actualize the position of the flow front with a vof method.

2.6. Discussion

The most important points that we wish to discuss here are the following

- As soon as we have chosen a model for the rheological behaviour of the polymer and that we are able to express it into the thermodynamical “standard” form, we are able to write a model for induced crystallization, which is “naturally” associated to this rheological model. A physical interpretation for this is that crystallization is related to the microscopic chain displacements and that the link between chain conformation and macroscopic mechanical is precisely the rheological constitutive relation. It can thus be understood that most of the induced crystallization mechanisms are already contained inside the rheology.
- This is not the only way to do it. Doufas et al. for example in a similar spirit (generalized Hamiltonian systems) decide to introduce a specific coupling function aimed to fit at best the crystallization kinetics. In case of necessity, we could do the same in our formalism, but we present here the simplest models.
- This formalism allows one to achieve numerical simulations. Injection moulding is simulated for example with the Pom–Pom model. Numerical procedure is described in [12]. Fig. 4 shows (for an advancing front coming from left side to right side), the evolution with time of the degree of crystallinity. At the end



Fig. 4. Degree of crystallinity during the injection moulding process.

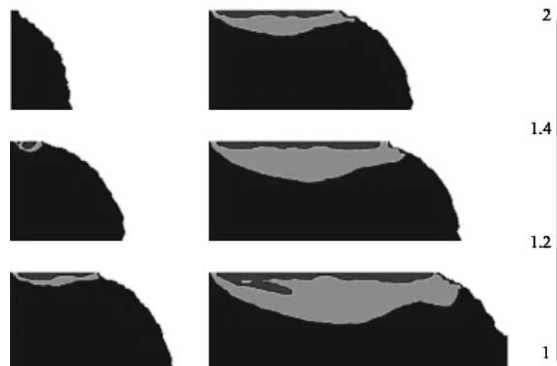


Fig. 5. Backbone stretch λ in injection moulding.

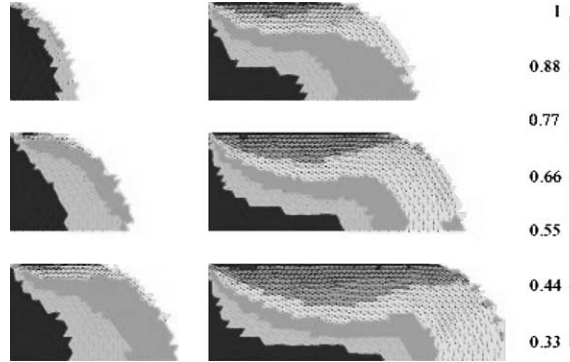


Fig. 6. Orientation tensor in injection moulding: arrows indicate the preferred orientation (eigenvector associated with the highest eigenvalue) and contours indicate t level of this maximum eigenvalue.

of the moulding stage (last picture), the skin layer begins to solidify and exhibits a crystallization affected by the flow. Fig. 5 shows for the same experimental situation, the evolution of the stretch λ . Here again the skin layer is predominantly stretched. Fig. 6 shows the orientation of the molecules. Near the flow front the fountain effects disorients the molecules, which are almost oriented near the walls.

3. Experimental

3.1. Biaxial tests

We briefly present here the biaxial set up (Fig. 7), which has been described in detail elsewhere [14]. The biaxial tests have been carried out on a triaxial testing machine named Astree (Fig. 7). Computer test control and data acquisition are performed by the object-oriented programming software, LabVIEW[®]. The material is a PET designed for blow-moulding (PET 99 21 W EASTMAN). Our cross-shaped specimens (Fig. 7) are injection-moulded, ensuring that the material is initially amorphous. In order to determine the strain field, black paint and random whites spots are sprayed over one of the specimens' surface, and the evolution of the spray pattern with time can be followed by a CCD camera associated

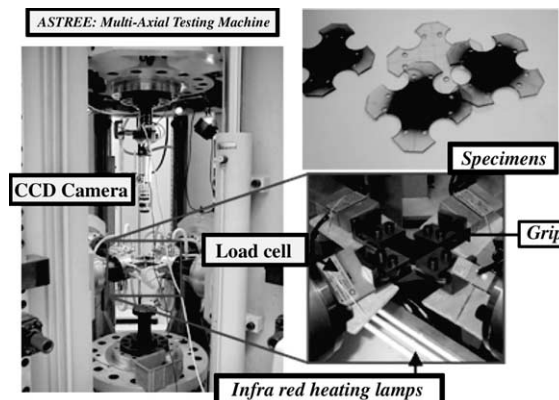


Fig. 7. Biaxial testing apparatus, triaxial testing machine Astree, biaxial specimens, IR heating apparatus.

with an image analysis software (OPTIMAS). The evolution in time of the strain field is then determined using a home-developed cross correlation technique [15], implemented in Matlab™. The accuracy of the method is at least on the order of 2/100 pixels and the smallest displacement detectable is also in the order of 2/100 pixels.

Like most polymers PET has low thermal conductivity. Heating techniques using convection or conduction not only require a long heating time, but also cause heterogeneity in the microstructure between the skin and the core of the material. An alternative is radiation heating with infrared waves. This method is commonly used in industry. The maximum variation of the temperature during a test is around $\pm 1^\circ$. The specimen is heated on one side only, leaving the opposite side available for image acquisition with a CCD camera. Since the grips are not translucent to infrared light, only the testing zone of the specimen is heated and deformed which prevents the polymer from shrinking and slipping in the grips. Two types of biaxial tension tests are carried out at different temperatures (90 and 100 °C) and elongation speeds (8, 20 and 40 mm/s). The first one is an equi-biaxial test in which the specimen is simultaneously stretched in the two perpendicular directions X_1 and X_2 (Fig. 8). The other type of bi-axial tests is sequential bi-axial: the

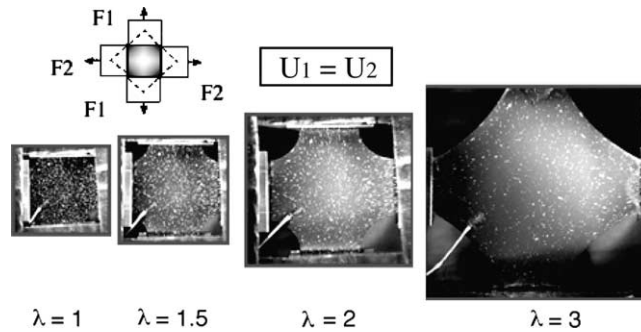


Fig. 8. Typical equi-biaxial elongation test.

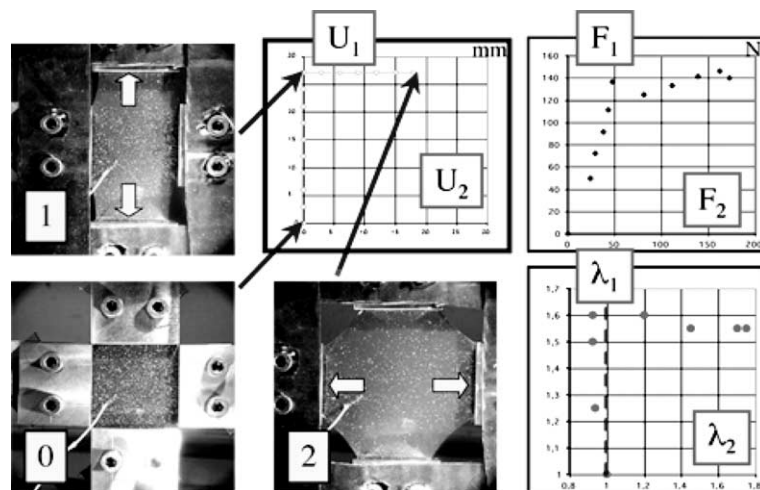


Fig. 9. Sequential biaxial loading, grip displacement U_1 and U_2 , load F_1 and F_2 and elongations in the central region of the specimen λ_1 and λ_2 .

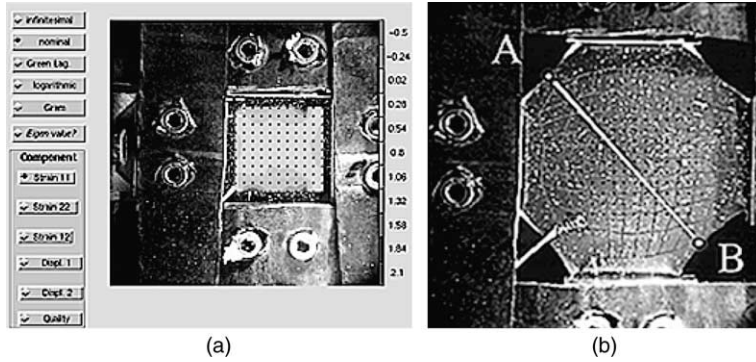


Fig. 10. Typical inter-correlation result for the equibiaxial test. (a) Typical displaced grid for equibiaxial testing, (b) ε_{11} nominal strain component.

specimen is stretched in the X_2 -direction first and then in the X_1 -direction (Fig. 9). Final draw ratios are the same for both types of tests.

Fig. 10 shows typical results obtained using Correli, our digital image correlation software. The displacement fields are clearly non-homogeneous in both biaxial tests.

3.2. Morphology analysis method

In a previous work [14], we showed that injected PET specimens presents no initial orientation and only low initial crystallinity ($\approx 3\%$). We also verified in that study that orientation (measured by IR dichroism) was homogeneous along the depth of the heated and stretched specimens and can thus be represented by only one variable f_c for the whole description of the specimen. This confirmed a posteriori the temperature homogeneity obtained by the infrared heating apparatus. Moreover, the study of thermal kinetics of PET confirmed that only very low thermal-induced crystallinity can develop in the tests carried out here.

WAXD experiments are undertaken using a Synchrotron radiation source (beamline D43 of LURE (Orsay, France)). The specimens are scanned using a monochromated beam with a wavelength of 1.45 \AA and a diameter of 0.5 mm . The sample to detector distance is 80 mm . Although no in situ measurements were carried out in this study, synchrotron radiation is still valuable because it makes it possible to measure thick specimens, which have seldom been studied. Moreover, it does not require any corrections due to X-ray mass attenuation for different thicknesses. The Debye–Scherrer patterns obtained are used to determine both the chain orientation and the crystallite geometry. The unit cell we choose is the one determined by Daubeny et al. [16]. The crystalline ratio can be inferred from the diffraction patterns, for example from the (010) crystal reflection peak area or the global comparison of amorphous and crystallized profiles. However, such methods have turned out to be less accurate than the density measurement technique, which we chose. The $(\underline{1}05)$ crystallographic plane, whose normal is close to the chain axis direction is studied. To determine the orientation in the whole volume, a study along the depth is necessary to take the out-of-plane rotation into account. As the scattering vector remained perpendicular to the specimen face, we could only get an evaluation of the orientation function f_c . Assuming that benzene rings tend to lie down on the specimen plane and that chains remain mainly in the plane specimen, as noted elsewhere [17], this approximation seems to be coherent. We have also checked in a previous study [14] that orientation (measured by IR dichroism) was homogeneous along the depth of the heated and stretched specimens. The Hermann crystalline orientation function f_c was measured by azimuthal scanning of the $(\underline{1}05)$ equatorial reflection (at $2\theta = 39.6^\circ$) whose normal is close to the chain axis direction. Background intensity was measured at the tail ends and then subtracted. The average cosine square angle $\langle \cos^2 \phi_{\underline{1}05} \rangle$ (with ϕ the angle

between the normal to ($\underline{1}05$) planes and the draw direction) was calculated from the corrected azimuthal intensities $I(\phi)$:

$$\langle \cos^2 \phi_{\underline{1}05} \rangle = \frac{\int_0^{\pi/2} I(\phi) \cdot \sin \phi \cdot \cos^2 \phi \cdot d\phi}{\int_0^{\pi/2} I(\phi) \cdot \sin \phi \cdot d\phi}.$$

We assume that $\langle \cos^2 \phi_{\underline{1}05} \rangle$ is close to $\langle \cos^2 \phi_c \rangle$ the average cosine square of the angle between the c-chain axis and the draw direction. The crystalline orientation derives then from the Hermann orientation relationship:

$$f_c = \frac{3\langle \cos^2 \phi_c \rangle - 1}{2}.$$

Fig. 11 shows the method used to determine the local orientation of the chains. Fig. 5a represents a typical oriented WAXD pattern on which we have marked the crystallographic reflections. A half-quarter circular zone is scanned along the azimuth angle. Compared to some of the other reflections the intensity of the ($\underline{1}05$) reflection is too low to be seen on the WAXD pattern. Nevertheless, the integrated intensity azimuthal profile is large compared to the noise and can be used to calculate the orientation function. Fig. 5b represents the integrated intensity and we can see that the peak is right on the 2θ angle calculated from the Bragg relation ($2\theta = 39.57^\circ$). Fig. 5c shows a slice of the integrated pattern for $2\theta = 39.57^\circ$. This profile (when background contribution is subtracted) can be used to calculate $\langle \cos^2 \phi_{\underline{1}05} \rangle$ and then f_c . The azimuthal scans were performed thanks to the Fit2D software developed by the European Synchrotron Radiation Facility (ESRF).

The X-ray diffraction pattern also allows a quantitative study of the crystal lamellar morphology through a 2θ integration. The 2θ integrated profile of amorphous specimen is subtracted from the stretched ones. The profile is then deconvoluted using a curve fitting program and the peaks are analyzed as PEARSON VII curves. The crystallographic planes investigated here are mainly ($\underline{1}05$) whose plane normal is close to the chain axis direction, (100) whose plane normal is close to the benzene ring normal, and (010). The reflections corresponding to these planes are pointed out in Fig. 11. Where the intensity of the

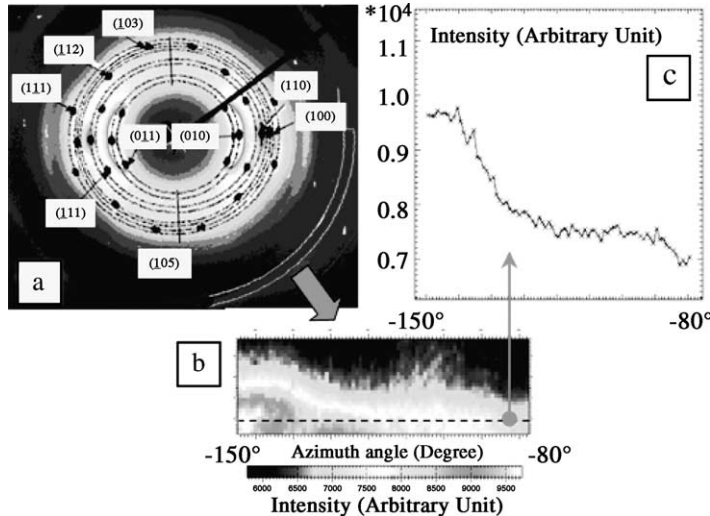


Fig. 11. Azimuthal scanning method. (a) WAXD pattern showing crystals reflections and the zone scanned, (b) azimuthal scan presenting intensity versus 2θ and azimuth angles, (c) profile obtained from a slice of the azimuthal scan for $2\theta_{\underline{1}05} = 39.6^\circ$.

reflection was too weak, we used the $(\underline{1}03)$ reflection whose plane normal direction is close to that of $(\underline{1}05)$. The crystal size along the directions normal to these planes are then calculated using the Scherrer relationship:

$$L_{hkl} = \frac{\lambda}{\cos \theta_{hkl} \cdot \Delta\theta_{hkl}},$$

where $\Delta\theta_{hkl}$ is the angular width inferred from the deconvolution analysis. The crystallite size calculated seems to be large enough to avoid corrections due to artificial peak broadening [18]. In a recent paper [19] the best choice for the lower crystal lamellar size is discussed, and was determined as being either the crystal thickness (here normal to (010) plane) or the result the $(0\underline{1}1)$ reflection. Yet, since the study using deconvolution remains difficult, especially in the case of oriented triclinic crystals such as PET, the difference between these two definitions is hardly noticeable. Moreover, given that the Scherrer relationship underestimates the lamellar size, a study along the (010) plane should give satisfactory average results.

3.3. Results and discussion

3.3.1. Crystallinity ratio

Fig. 12 shows crystallinity measurements undertaken on samples cut off from the central zone of specimens subjected to biaxial elongation tests. ‘‘High strain’’ refers to an elongation ratio λ of about 3 and ‘‘low strain’’ to an elongation ratio λ of about 2. As is well known in uniaxial elongation case, crystallization begins when a minimum strain has been reached. The critical elongation seems to be close to the one observed in the uniaxial case. Strain hardening and an increase of crystallinity appear during the second stage of elongation: typically above $\lambda = 2$. For the high strain test, the top-right chart in Fig. 6 shows the influence of strain rate: final crystallinity increases with speed. Of course this correlation saturates for very high tension speeds since the ultimate crystallinity ratio is an upper bound. In the chart in the bottom-left, the effect of temperature is illustrated on two sequential biaxial tests. This result has also been observed on equibiaxial tests: as temperature increases, induced crystallinity decreases. The last chart (bottom-right) compares equibiaxial and sequential biaxial tests. This final observation has to be confirmed, since it is very difficult to obtain the same final strain field for both kinds of tests. It seems that initial orientation during the first stage of the sequential biaxial test helps to induce crystallization during the second stage. The sequence leads to a higher final crystallinity ratio.

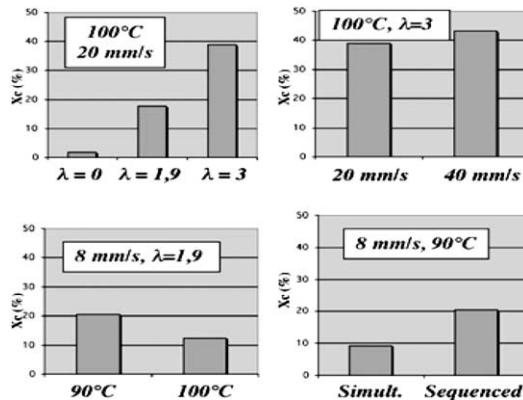


Fig. 12. Influence of elongation, strain rate, temperature and strain sequence on induced-crystallization ratio.

3.3.2. Molecular orientation

Fig. 13 associates a macroscopic heterogeneous displacement and deformation field with the induced microstructure measured in different zones of the specimen during a simultaneous biaxial stretching test. As expected, the chains are strongly oriented along the draw direction in zones 1 and 2, where the strain is almost plane. In the central zone, where the strain is nearly equibiaxial, no preferential orientation can be seen ($f_c \approx 0$). In the diagonal region, the chains are strongly oriented in the 45° direction, which is consistent with the fact that this corresponds to a shear strain zone. The measured orientations seem actually very close to the stress curves expected (linked to the conformation tensor) for this simultaneous test. So, as has been reported recently [8,20,21], for ex situ as well as in situ study, the chains orientation seems only slightly tilted through relaxation above a critical strain ratio, which is also confirmed by the little deviation (about 10°) of the equatorial reflections. This behaviour could be explained by the strain-induced crystallization which could “lock” the chain relaxation. This hypothesis is also supported by the high crystallinity ratio observed, although the latter might have been increased through relaxation.

And indeed, if we assume that the retraction and reptation molecular times are close for uniaxial and biaxial cases, a comparison with a recent study by Mahendrasingam et al. [20] shows that an experiment undertaken in our conditions (strain rate and temperature) should lead to some crystallisation occurring during the deformation, which could also confirm the lock-in of the chains conformation.

Figs. 14 and 15 show how experimental parameters (strain rate and ratio, temperature, strain sequence) can influence WAXD patterns. In these figures, we find again the same behaviour that we have already discussed, i.e. there is a critical draw ratio and strain rate and temperature have opposite effects, which is also clearly observed in situ [22]. It should be noticed that for sequential tests, the molecular chains remain oriented along the first stretching direction as reported elsewhere for biaxial stretching of PET films [23],

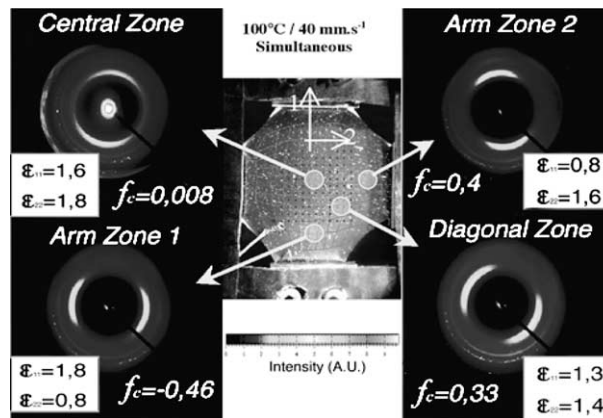


Fig. 13. Chain orientation at different points on the specimen.

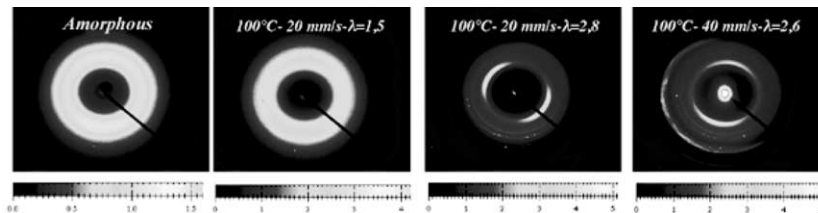


Fig. 14. Influence of strain ratio and rate on molecular orientation and size of crystallites.

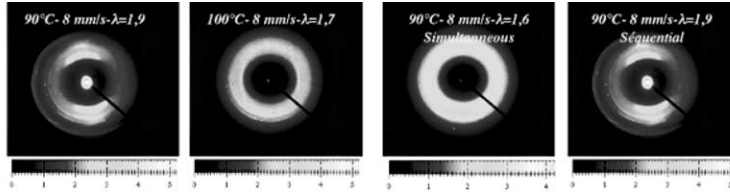


Fig. 15. Influence of temperature and type of sequence path on molecular orientation and size of crystallites.

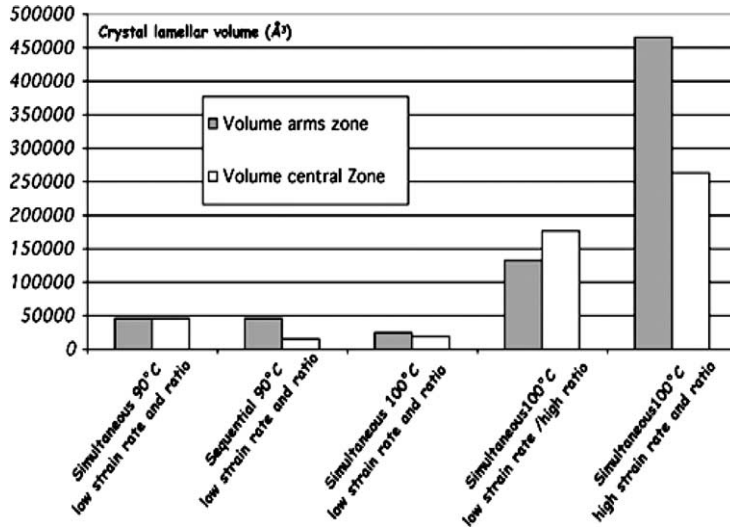


Fig. 16. Evolution of crystal lamellae volume in different experimental conditions.

probably because the stretching along the second direction is not strong enough (low ratio) to break down the crystalline blocks and shift the orientation.

3.3.3. Crystal lamellar size

Two different regions of the specimens are studied, the central one where the elongation is equibiaxial and the ones near the grips where the elongations are close to those of a plane strain case (Fig. 13). Knowing the size of the crystal along three independent directions allows us to gauge its volume. Fig. 16 represents the change in volume of the lamellar crystal in different experimental conditions. For low strains, the crystallites remain small at the two temperatures tested, whatever the strain rate. The opposite effects of temperature and strain rate can once again be observed. These tendencies are verified for both biaxial and plane strain zones. When the strain rate rises above a critical strain ratio, the volume of the crystallites increases very significantly. This is mainly caused by an important growth of lamellae along the chain axis as strain rate increases, and also by the fact that the length of the crystals along the (1 0 0) direction seems very sensitive to the draw ratio. It is worth noting that the growth of crystal lamellae along the chain axis is higher in “plane-strain” zones than in the equibiaxial one. The lower length observed here is along the (0 1 0) direction. This “thickness” is almost independent on the draw ratio, and the strain rate. The values for both kinds of zones are close and no influence of strain type can be seen. A possible explanation for these weak dependencies could be that an equilibrium has been reached, depending mainly from the stretching temperature.

If we compare the volume of the crystals to the crystallinity ratio measured it is possible to evaluate the average number of crystals per unit volume [7]. This shows the importance of the type of strain and history experimented by the material. For example, sequential tests lead to smaller but more numerous crystals, and there are even more of them in the equibiaxial strain zone. This illustrates the crumbling of the crystal blocks generated by the second stretching even if, as noted previously, the draw ratio was too low to change the former orientation. For high strain ratios, one can see that a higher strain rate generates bigger but fewer crystals, differs from the in situ observations [22] where the halfwidth of the crystalline reflection seemed to remain essentially unchanged during the crystallization process. This could be explained by a higher orientation during the stretching phase and more amorphous material converted into crystal during the relaxation [21].

4. Conclusions

We have presented in this paper a theoretical and experimental investigation into the mechanical behaviour of a thermo-plastic undergoing both deformation and crystallization. Our theoretical model was developed in the general framework of irreversible thermodynamics. Such formalism is known to be appropriate to be implemented in finite element codes and to solve for complex thermo-mechanical conditions as it is generally the case in practical situations. Our model is a macroscopic one, but it explicitly takes into account the behaviour of the material at molecular scale. A limited number of adjustable parameters are then needed, which would reinforce the predictability of the model. An additional advantage of the model developed here is the possibility of dealing with both shear and elongation, or any other complex strain field. Experiments investigating the behaviour of the material at molecular scale are needed in order to validate the model. In the present study, we considered the PET subjected biaxial elongation. The strain field was determined using an image correlation technique, and the microstructure analyzed using the WAXD technique. The later allowed us to undertake crystalline texture characterization, including crystallinity ratio, the crystallite orientation and the size of the crystallites. In order to infer molecular orientation and stretching, we need to use other techniques such as optical polarimetry (birefringence and dichroism). This is currently under study.

The comparison between our model and the experiments above is still under investigation and will be presented elsewhere.

Acknowledgements

To EASTMANN for providing us with the PET, to G. Régnier who allowed their injection and to J. Doucet for his help in the X-ray diffraction experiments.

References

- [1] A. Poitou, A. Ammar, C.R. Acad. Sci. 329 II b (2001) 5–11.
- [2] Y. Marco, L. Chevalier, M. Chaouche, Polymer 43 (24) (2002) 6569–6574.
- [3] F. Jay, B. Monasse, J.M. Haudin, Int. J. Form. Proc. 1 (1998) 75–95.
- [4] G. Titomanlio, V. Speranza, Int. Polym. Proc. 12 (1) (1997) 45–53.
- [5] S. Liedauer, G. Eder, H. Janeshitz-Kriegl, Int. Polym. Proc. 10 (3) (1995) 269–342.
- [6] A.K. Doufas, I.S. Dairanieh, A.J. McHugh, J. Rheol. 43 (1) (1999) 85–109.
- [7] M. Vigny, J.F. Tassin, A. Gibaud, G. Lorentz, Polym. Engrg. Sci. 37 (1998) 1785–1794.
- [8] E. Gorlier, J.M. Haudin, N. Billon, Polymer 42 (2001) 9541–9549.

- [9] A. Mahendrasingam, C. Martin, W. Fuller, D.J. Blundell, D.H. MacKerron, J. Oldman, J.L. Harvie, R.C. Riekkel, P. Engström, *Polymer* 40 (1999) 5553–5565.
- [10] J.A. Pople, G.R. Mitchell, S.J. Sutton, A.S. Vaughan, C.K. Chai, *Polymer* 40 (1999) 2769–2777.
- [11] G. Bishko, T.C.B. McLeish, O.G. Harlen, R.G. Larson, *Phys. Rev. Lett.* 79 (1997) 2352–2355.
- [12] A. Ammar, Ph.D. Thesis, ENS de Cachan France, 2001.
- [13] H.C. Ottinger, XIIIth Intern. Congress on Rheology, Cambridge, UK, 2000.
- [14] Y. Marco, L. Chevalier, G. Régnier, A. Poitou, *Macromolecular Symposia*, special issue on FICOP, 2001.
- [15] L. Chevalier, S. Calloch, F. Hild, Y. Marco, *Eur. J. Mech. A/solids* 20 (2001) 169–187.
- [16] R.P. Daubeny, C.W. Bunn, C.J. Brown, *Proc. Roy. Soc. Lond. A* 226 (1954) 531–542.
- [17] U. Göshel, K. Deutscher, V. Abetz, *Polymer* 37 (1996) 1.
- [18] A. Guinier, *Théorie et technique de la radiocristallographie*, Dunod, 1956, pp. 463–489.
- [19] Z.G. Wang, B.S. Hsiao, B.X. Liu, F. Yeh, B.B. Sauer, H. Chang, J.M. Schultz, *Polymer* 41 (2000) 1791–1797.
- [20] A. Mahendrasingam, C. Martin, W. Fuller, D.J. Blundell, R.J. Oldman, D.H. MacKerron, J.L. Harvie, R.C. Riekkel, *Polymer* 41 (2000) 1217–1221.
- [21] R.G. Matthews, A. Aji, M.M. Dumoulin, R.E. Prud'homme, *Polymer* 41 (2000) 7139–7145.
- [22] D.J. Blundell, A. Mahendrasingam, C. Martin, W. Fuller, D.H. MacKerron, J.L. Harvie, R.J. Oldman, C. Riekkel, *Polymer* 41 (2000) 7793–7802.
- [23] M. Vigny, J.F. Tassin, G. Lorentz, *Polymer* 40 (1999) 397–406.